



CO₂ capture and photocatalytic reduction using bifunctional TiO₂/MOF nanocomposites under UV-vis irradiation

Angus Crake ^a, Konstantinos C. Christoforidis ^a, Andreas Kafizas ^b, Spyridon Zafeiratos ^c, Camille Petit ^{a,*}

^a Barrer Centre, Department of Chemical Engineering, Imperial College London, South Kensington Campus, London SW7 2AZ, UK

^b Department of Chemistry, Imperial College London, South Kensington Campus, London SW7 2AZ, UK

^c Institut de Chimie et Procédés Pour l'Energie, l'Environnement et la Santé, (ICPEES) ECPM, University of Strasbourg, 25 rue Becquerel Cedex 2, Strasbourg, France



ARTICLE INFO

Article history:

Received 16 December 2016

Received in revised form 14 February 2017

Accepted 13 March 2017

Available online 16 March 2017

Keywords:

Metal-organic frameworks

Titanium dioxide

Photocatalysis

Carbon dioxide

Reduction

ABSTRACT

TiO₂ nanosheets and metal-organic framework (NH₂-UiO-66) were effectively coupled *via* an *in-situ* growth strategy to form bifunctional materials for the combined capture and photocatalytic reduction of CO₂ under UV-vis light irradiation. This was done to take advantage of the high CO₂ adsorption capacity of the MOF and the photocatalytic properties of pre-formed TiO₂ nanosheets in a single material. The prepared materials were thoroughly characterized using a variety of techniques. They were subsequently tested for CO₂ adsorption and CO₂ photocatalytic reduction using a heterogeneous gas/solid set-up to imitate both CO₂ capture and fixation in a single process. The adopted synthesis process allowed the development of a tight interaction between TiO₂ and NH₂-UiO-66 forming a heterojunction, while maintaining both the high CO₂ uptake and porosity of NH₂-UiO-66. The nanocomposites were proven durable and significantly more efficient in reducing CO₂ to CO than their single components. Photocatalytic activity was greatly affected by the nanocomposites composition with the optimum TiO₂ content doubling the CO evolution rate compared with the pure TiO₂. The improved photoactivity was assigned to the enhanced abundance of long lived charge carriers, as revealed by transient absorption spectroscopy (TAS). This most likely occurred due to the effective charge transfer *via* interface. A possible mechanism is discussed on the basis of the combined catalytic, spectroscopic and CO₂ adsorption results.

© 2017 Elsevier B.V. All rights reserved.

1. Introduction

Predictions of global energy usage suggest continued increase in carbon emissions unless major changes are made to the way energy is produced and used. The current rate of global carbon emission is about 8 GtC per year and is predicted to increase to nearly 26 GtC per year by 2100 with CO₂ concentration levels now exceeding 390 ppm [1]. These numbers leave little doubt that carbon management and renewable energy must play important roles in our future energy outlook. Hence, the development of efficient carbon capture, utilization and storage (CCUS) technologies is one of the greatest challenges faced by mankind [2].

As part of the capture step, amine scrubbing, oxyfuel combustion and calcium looping have reached a maturity suitable for commercial application, but would all impose large energy penal-

ties [3]. In parallel to these proposed technologies, the use of solid adsorbents has been explored owing to their ability to capture CO₂ at low temperatures in a potentially less energy demanding process. Among other materials investigated, metal-organic frameworks (MOFs) have emerged as an exciting potential CO₂ adsorbent [4]. MOFs are a class of crystalline and porous materials formed by a network of metal ions or metal clusters linked by polydentate organic molecules *via* strong metal-ligand coordination bonds. They are particularly promising materials due to their structural tunability, high surface area, high and selective CO₂ adsorption capacity [5].

Another interesting development as part of Carbon Capture Utilization and Storage (CCUS) research is the use of captured CO₂ as chemical feedstock (i.e. CO₂ utilization). CO₂ conversion to chemicals (e.g., syngas, methane, methanol and formic acid) *via* chemical, electrochemical or photochemical reactions has been proposed and significant efforts are being carried out in this field [6]. However, chemical fixation of CO₂ remains a very challenging endeavor mostly due to the inert nature of CO₂ [6]. Among the different

* Corresponding author.

E-mail address: camille.petit@imperial.ac.uk (C. Petit).

methods suggested so far [7], photocatalytic conversion of CO₂ into value-added chemicals enables the utilization of an endless and free energy (i.e. solar energy). Therefore, it has inspired extensive research since the process was first demonstrated in 1979 [8–10]. Semiconductors were the first, and remain, the most extensively investigated materials as photocatalysts. Among them, TiO₂ materials are the most widely investigated photocatalysts due to their high stability, low cost and non-toxic nature [11–13]. Pure TiO₂ and TiO₂-based composites of various configurations, composition and morphology at the nanoscale have been synthesized and applied in CO₂ photoreduction [14–18]. Overall, studies on TiO₂ have shown that photocatalytic activity is drastically affected by the exposed TiO₂ facets. In the specific case of CO₂ reduction, an optimal 58% of exposed (001) facets in pure anatase TiO₂ was reported by Yu et al. [14]. Nevertheless, catalytic efficiency is not yet at acceptable levels. The weak CO₂ adsorption on the catalyst surface contributes partially to this end. [15]

Recently, MOFs have also been explored in this field [19,20]. However, the photoactivity of MOFs is not comparable to that of inorganic semiconductors mostly due to the low photogenerated charge formation and low charge separation efficiency. In this regard, pre- and post-synthesis modifications have been made [21,22]. Among the MOFs tested, NH₂-UiO-66 has attracted notable attention due to its chemical stability and visible light adsorption [23–26]. Targeting improved efficiencies, MOFs have been effectively coupled with other photocatalysts [24,27–29]. Metal complexes have been effectively integrated into MOFs structures and applied either as catalysts for direct CO₂ reduction [30] or visible light sensitizers to activate the MOF [31]. In addition, TiO₂ particles have been grafted onto preformed HKUST-1 microcrystals by hydrolysis to create a TiO₂/HKUST-1 composite [27]. More recently, TiO₂ nanoparticles were grown on Co-ZIF-9 and the prepared composites were applied for CO₂ photoreduction under UV-vis light irradiation [32]. Studies have also shown that the establishment of synergistic effects leading to improved activity is greatly affected by the nature of the coupled materials. For example, CO₂ reduction was significantly improved when CdS was coupled with Co-ZIF-9 while the reaction did not proceed when NH₂-UiO-66 was used instead [24]. The interaction between semiconductors and MOFs was identified as the critical parameter for enhanced photoactivity [32,33]. This is directly linked with a charge transfer process between semiconductors and MOFs suppressing electron-hole recombination process [27–29,32].

In the present study, we report the development of novel bifunctional TiO₂/MOF nanocomposites for the combined capture and photocatalytic reduction of CO₂. The TiO₂ component was selected for its photocatalytic activity while the MOF component was hypothesized to enhance CO₂ uptake and provide the pore space needed to promote access to the catalytic sites. In an effort to better control in parallel both the TiO₂/MOF interaction as well as the activity of the TiO₂ part, an *in-situ* synthesis process was adopted for the first time to develop NH₂-UiO-66 in the presence of pre-synthesized large TiO₂ nanosheets (NS) with exposed (001) facets. Unlike other contributions, herein the shape and the exposed facets of the TiO₂ were controlled. The MOF content was controlled and the materials were applied for CO₂ adsorption and photoreduction under ambient conditions in a heterogeneous gas/solid set-up in an attempt to imitate both CO₂ capture and fixation in a single process (most prior studies use a gas/liquid set-up). To provide an in-depth investigation of the mechanisms of reactions and further advance research in this field, a combination of several analytical and spectroscopic techniques were used. The prepared nanocomposites were proven significantly more active than the single components and this was attributed primarily to the enhanced formation of long lived photogenerated charges.

2. Experimental

2.1. Material synthesis

All reagents used in this study were of analytical grade and used without further purification. 1,2-aminoterephthalic acid (99%), hydrochloric acid (HCl, 37%), hydrofluoric (48%), titanium butoxide (97%), and zirconium (IV) chloride (ZrCl₄, 99.5%) were purchased from Sigma-Aldrich. N,N-Dimethyl formamide (DMF, 99.9%, anhydrous) was purchased from VWR.

2.1.1. Synthesis of TiO₂ nanosheets (NS)

TiO₂ NS were prepared through a solvothermal method [34]. 30 mL of titanium butoxide were added into a Teflon cup. Then, 3 mL of HF (48%) were slowly added into the above solution under stirring. The mixed solution was magnetically stirred for 10 min and then the Teflon cup was sealed in a stainless steel autoclave and placed in an oven at 180 °C for 24 h. After that, the autoclave was naturally cooled to room temperature, the white solid was collected, separated and washed with deionized water and ethanol by centrifugation three consecutive times. The powder was dried overnight at 65 °C, vacuum treated at 120 °C and finally calcined at 300 °C for 4 h under static air in order to remove any remained organics.

2.1.2. Synthesis of NH₂-UiO-66

NH₂-UiO-66 was synthesized based on a previously reported procedure [35] and scaled up to increase product yield. Briefly, 1.25 g of zirconium (IV) chloride (ZrCl₄, 99.5%, Sigma-Aldrich), 50 mL N,N-Dimethyl Formamide (DMF, 99.9%), and 10 mL concentrated hydrochloric acid (37%) were combined in beaker and placed in a sonication bath for 20 min. 1.34 g of 1,2-aminoterephthalic acid (99%) and additional 100 mL DMF were added. The mixture was sonicated for 20 min, transferred to a round bottom flask, and then heated under stirring to 150 °C for 24 h in an oil bath. After cooling, the solid particles were recovered by centrifugation and washed three times with ethanol, vacuum dried at 120 °C and then stored in a desiccator.

2.1.3. Synthesis of TiO₂/NH₂-UiO-66 composites

For the synthesis of the nanocomposites, an *in-situ* approach was adopted for the development of NH₂-UiO-66 in the presence of pre-synthesized TiO₂ NS in order to allow a greater contact between the two components as this was shown to favor charges separation in a prior study [32,33]. The synthesis was based on the pure NH₂-UiO-66 synthesis process. A fixed amount of TiO₂ (0.5 g) was sonicated for 30 min in DMF. The TiO₂ content in the nanocomposites was controlled by scaling the NH₂-UiO-66 synthesis. Herein, the NH₂-UiO-66 sample is referred to as MOF and the obtained nanocomposites are named x-TiMOF, where an increase x (x = 1, 2, 3, 4) denotes an increase in NH₂-UiO-66 content (from 19 to 37 wt.%).

2.2. Materials characterisation methods

Thermogravimetric analysis (TGA) was carried out under a nitrogen flowrate of 100 mL min⁻¹, from 25 to 900 °C at a heating rate of 10 °C min⁻¹ using a Netzsch TG 209 F1 Libra instrument. Samples were stored in a vacuum oven at 120 °C for 24 h prior to TGA.

X-ray diffraction measurements were performed with a PANalytical X'Pert PRO instrument at room temperature (reflection mode at 40 kV and 40 mA using Cu K α radiation ($\alpha_1 = 1.54057 \text{ \AA}$, $\alpha_2 = 1.54433 \text{ \AA}$, weighted average = 1.54178 \AA).

Attenuated total reflection Fourier transform-infrared (ATR-FTIR) spectra were collected at room temperature using a Perkin-Elmer Spectrum 100 Spectrometer equipped with an ATR

cell. The spectra were generated, collected 8 times, and corrected for the background noise. The experiments were done on the powdered samples, without KBr addition.

The X-ray photoelectron spectroscopy (XPS) measurements were carried out in an ultrahigh vacuum (UHV) spectrometer described elsewhere [36]. The Al K α line (1486.6 eV) of a dual anode X-ray source was used as incident radiation. Survey and high resolution spectra were recorded in constant pass energy mode (44 and 22 eV, respectively). Since the C 1 s peak contains contribution of organic residuals related to the synthesis of the materials it cannot be used to correct the binding energy scale, as is typically done with adventitious carbon. Therefore, we have used F 1 s (from HF) and N 1 s (from DMF) as internal standards of TiO₂ and MOF respectively to correct the BE scale of the presented XPS spectra. Spectra fitting was performed with the CasaXPS software using Ti 2p and Zr 3d line shapes recorded on TiO₂ and NH₂-UiO-66 samples as reference peaks. The peak position and width was constrained to that of the reference spectra during the fitting process. Elemental atomic concentrations were obtained by dividing the areas of the photoelectron peaks with literature atomic sensitivity factors and assuming a homogeneous distribution arrangement model. Please note that quantification is not expected to give accurate absolute elemental composition results due to uncertainties related to the sample morphology, but allows relative comparison of the samples.

Scanning electron microscopy (SEM) images were taken using a high resolution LEO Germini at 1525 at 5 kV in secondary electron mode (InLens detector). Energy-dispersive X-ray (EDX) spectroscopy was performed using an Oxford Instruments silicon drift detector. Prior to analysis, the samples were ground and mounted on carbon tape and coated with 20 nm chromium.

Nitrogen adsorption and desorption isotherms were measured using a Micrometrics 3Flex sorption analyser at -196 °C. The surface area was calculated from the Brunauer-Emmett-Teller method [37]. The total volume of pore was calculated from the volume adsorbed at P/P₀ = 0.97. The volume of micropores was determined using the t-plot method. The volume of mesopores was calculated as the difference between the total pore volume and the volume of micropores. CO₂ sorption was also evaluated up to 1 bar using the same instrument at 25 °C. Prior to the measurements the samples were degassed at 0.2 m Torr, 120 °C for 24 h.

Diffuse reflectance ultraviolet-visible (DR-UV/Vis) was measured using a Agilent Cary 500 UV-vis-NIR spectrometer equipped with an integrating sphere. Spectral band width was set to 2 nm, with Spectralon as a standard. The samples were compressed onto a KBr backed pellet for analysis. Spectra were treated using Kubelka-Munk function [38] in order to eliminate any tailing contribution from the DR-UV-vis spectra. The following equation was applied:

$$F(R) = \frac{(1 - R)^2}{2R}$$

where R is the reflectance. The band-gap (E_g) values were estimated from the plot of $F(R)hv^{1/2}$ versus energy by extrapolating the linear part.

2.3. Transient absorption spectroscopy

Transient absorption spectroscopy, from the microsecond to second timescale, was measured in a diffuse reflection mode. A Nd:YAG laser (OPOTEK Opolette 355 II, 7 ns pulse width) was used as the excitation source, generating 355 nm light from the third harmonic transmitted to the sample through a light guide. An excitation power density of ~2 mJ cm⁻² and laser repetition rates of 0.6 Hz was used. As the photo-induced changes in reflectance were low (< 1%), it was assumed that the transient signal was directly proportional to the concentration of excited species. The probe light was a 100 W Bentham IL1 quartz halogen lamp. Long pass filters

(Comar Instruments) were placed between the lamp and sample to minimize short wavelength irradiation of the sample. Diffuse reflectance from the sample was collected by a 2" diameter, 2" focal length lens and relayed to a monochromator (Oriel Cornerstone 130) to select the probe wavelength. Time-resolved intensity data was collected with a Si photodiode (Hamamatsu S3071). Data at times faster than 3.6 ms was recorded by an oscilloscope (Tektronics DPO3012) after passing through an amplifier box (Costronics), whereas data slower than 3.6 ms was simultaneously recorded on a National Instrument DAQ card (NI USB-6251). Each kinetic trace was obtained from the average of between 100 and 250 laser pulses. Acquisitions were triggered by a photodiode (Thorlabs DET10A) exposed to laser scatter. Data was acquired and processed using home-built software written in Labview. Experiments were carried out in diffuse reflectance, since the materials were highly light scattering. In a typical experiment, a UV laser (355 nm, ~2 mJ cm⁻²) was used to photoexcite our nanopowder. Transient changes in diffuse reflectance were then measured in the visible region between 500 and 900 nm [39].

2.4. Photocatalytic CO₂ reduction

A gas/solid reactor setup was assembled as illustrated in Fig. S1. The photocatalysts were deposited on a glass slide with a fixed area of 4.5 cm². Research grade (99.99%) CO₂ and H₂ (99.999%, Peak Scientific PH200 hydrogen generator) were flowed at controlled rates using mass flow controllers (Omega Engineering, 0–50 mL/min). Firstly, the photoreactor (132 mL) was vacuumed and replenished with CO₂ and H₂ five times. Then, CO₂ and H₂ (1.5 vol/vol ratio) was passed over the catalyst bed in the photoreactor for 15 residence times before it was sealed at 1.15 bara. A xenon arc lamp (150 W, $\lambda > 325$ nm, LOT Quantum Design), equipped with a water filter was used as the irradiation source. Evolved gases were detected by a gas chromatograph (GC, Agilent Technologies) with hayesep and mol sieve columns in series, thermal conductivity (TCD) and flame ionisation (FID) detectors. To assess the stability of the photocatalysts, the process above was repeated after each 6 h illumination without opening the photoreactor.

3. Results and discussion

3.1. Characterization of the chemical and structural features of the materials

TGA was first used to quantify the TiO₂ and NH₂-UiO-66 contents in the nanocomposites and assess their thermal stability. It can be seen from Fig. S2 that TiO₂ was stable up to 900 °C. The small mass drop from 300 to 700 °C of 2.8 wt% can be attributed to impurities from the TiO₂ synthesis as this material was calcined at 300 °C. NH₂-UiO-66 exhibited stability up to around 200 °C. The lack of mass drop prior to this shows no detectable guest species (i.e. DMF) remaining in the pore network after synthesis. As expected, the organic ligands and hence the framework decomposed above 200 °C [35,40]. The thermal degradation profiles of TiO₂/NH₂-UiO-66 nanocomposites displayed characteristics of both TiO₂ and NH₂-UiO-66, allowing the TiO₂ content to be quantified from the final residual mass (Table S1). The TiO₂ content of the composites ranged from 63.2 to 81.0 wt% and increased as TiO₂/NH₂-UiO-66 synthesis ratio increased.

XRD was then used to verify the formation of both the TiO₂ and NH₂-UiO-66 components in the composites. Fig. 1 presents the XRD patterns of the pure TiO₂ and NH₂-UiO-66 materials and the x-TiMOF composites. All samples showed high levels of crystallinity. In the case of TiO₂ only anatase (A) phase was detected [41]. NH₂-UiO-66 displayed the typical diffraction pattern of that

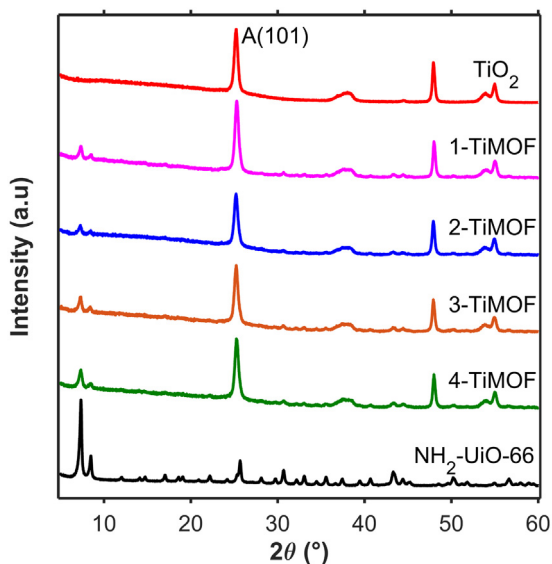


Fig. 1. XRD patterns of TiO_2 , $\text{NH}_2\text{-UiO-66}$ and $\text{TiO}_2/\text{NH}_2\text{-UiO-66}$ nano composites ($x\text{-TiMOF}$) confirming the presence of the two phases in the composites.

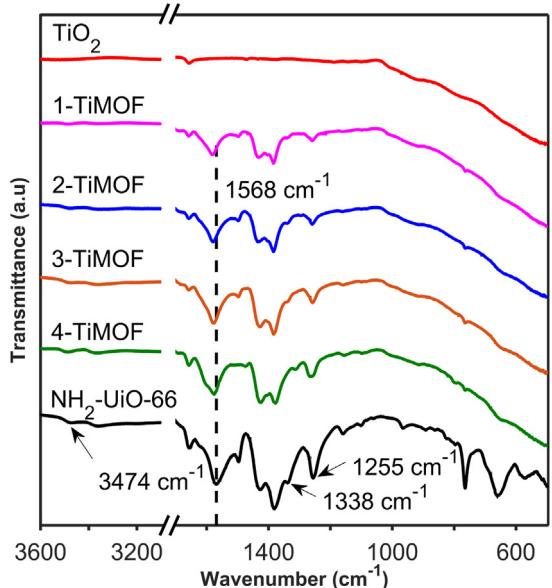


Fig. 2. ATR-FTIR of TiO_2 , $\text{NH}_2\text{-UiO-66}$ and $\text{TiO}_2/\text{NH}_2\text{-UiO-66}$ nanocomposites ($x\text{-TiMOF}$).

particular MOF [23,25,26,35]. As evidenced by the XRD patterns of the $x\text{-TiMOF}$ composites, the phase composition and crystallinity of TiO_2 did not change after the synthesis process applied for the MOF nucleation and growth. Similarly, no obvious changes were detected in the diffraction peaks of the nanocomposites corresponding to the $\text{NH}_2\text{-UiO-66}$ part. In fact, the nanocomposites showed a combination of the TiO_2 and $\text{NH}_2\text{-UiO-66}$ patterns with intensity proportional to abundance. Hence, the XRD data provided direct evidence that both TiO_2 and $\text{NH}_2\text{-UiO-66}$ structures were present and not noticeably altered by the synthesis process applied for the development of the nanocomposites.

ATR-FTIR spectroscopy enabled to get a greater insight into the interactions between the two composite components (Fig. 2). The $\text{NH}_2\text{-UiO-66}$ and TiO_2 samples showed similar characteristics to those reported in literature [23,32,42]. Nevertheless, differences were detected for the $x\text{-TiMOF}$ nanocomposites when compared with the pure reference materials. Particularly, the $\text{NH}_2\text{-UiO-66}$

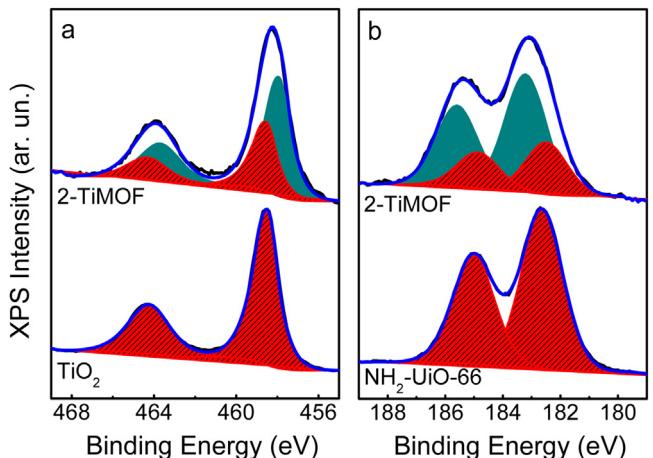


Fig. 3. Core level XPS spectra of the pure TiO_2 and $\text{NH}_2\text{-UiO-66}$ and 2-TiMOF nanocomposite in the: (a) Ti 2p and (b) Zr 3d regions. The appearance of additional Ti and Zr components in the composite suggests a modification in the surface chemical states and points to an interaction between the TiO_2 and $\text{NH}_2\text{-UiO-66}$.

66 bands at 1338 cm^{-1} and 1255 cm^{-1} corresponding to the $\text{C}_\text{ar}-\text{N}$ stretching vibration modes [43] decreased in intensity for the nanocomposites while the latter shifted to 1262 cm^{-1} . The $\text{NH}_2\text{-UiO-66}$ band centered at 1568 cm^{-1} assigned to the OCO asymmetric stretching vibration mode shifted to 1581 cm^{-1} for the composites. In addition, the intensity of the low frequency bands ($763-473 \text{ cm}^{-1}$), which are a combination of OH and CH bending and Zr–O modes, was significantly decreased in the nanocomposites. These changes suggest an alteration of the organic moiety ligation to the metal cluster [44]. Changes were also detected on the amine group bands. The band centered at 3474 cm^{-1} ascribed to the asymmetric N–H stretching vibration mode [45] shifted to 3487 cm^{-1} in the nanocomposites. Overall, the presence of $\text{NH}_2\text{-UiO-66}$ bands in the IR spectra of $x\text{-TiMOF}$ nanocomposites confirmed the presence of the MOF in the composites and suggested that the structural features of the MOF are maintained in the presence of TiO_2 . In addition, the observed changes compared with the pure $\text{NH}_2\text{-UiO-66}$ suggested the presence of interactions between the two components of the nanocomposites.

X-ray photoelectron spectroscopy (XPS) was employed to investigate the chemical state and the composition of the outermost surface (ca. 5 nm). The survey spectra confirmed the presence of Zr, Ti, O, N, and C elements (Fig. S3) while in case of pure TiO_2 and the nanocomposites F originating from HF used to synthesize TiO_2 , was also detected. The Ti 2p core level spectra of TiO_2 , and 2-TiMOF samples are shown in Fig. 3a. The Ti $2p_{3/2}$ binding energy (BE) for the pure TiO_2 sample was found at 458.5 eV in agreement with previous published results for Ti^{4+} in TiO_2 [46]. The Ti 2p spectrum of 2-TiMOF is shifted at lower BEs and has a broader line shape (the width of Ti $2p_{3/2}$ increases to 1.8 eV instead of 1.5 eV in the pure TiO_2). The analysis of the Ti 2p peak using two doublets with fixed spin-orbit splitting and $2p_{3/2}/2p_{1/2}$ area ratio, indicated an additional Ti 2p component at 457.9 eV . This new Ti component cannot be attributed to reduced Ti^{3+} species, since typically the BE of Ti^{3+} is reported around 457 eV or lower [46,47]. The Zr 3d peaks of $\text{NH}_2\text{-UiO-66}$ and 2-TiMOF samples are displayed in Fig. 3b. As in the case of Ti 2p, the Zr 3d core levels are split into two components, due to the spin-orbit coupling effect. The Zr 3d peak of $\text{NH}_2\text{-UiO-66}$ at 182.6 eV is characteristic of Zr^{4+} [48], while in case of 2-TiMOF the spectrum becomes broader and shifts to higher BEs. The fitting procedure indicates that this is due to the contribution of an additional Zr 3d peak at 183.2 eV . The appearance of the additional Ti and Zr components at 457.9 and 183.2 eV respectively, suggested a modification in the surface chemical states of Zr and Ti in the composite

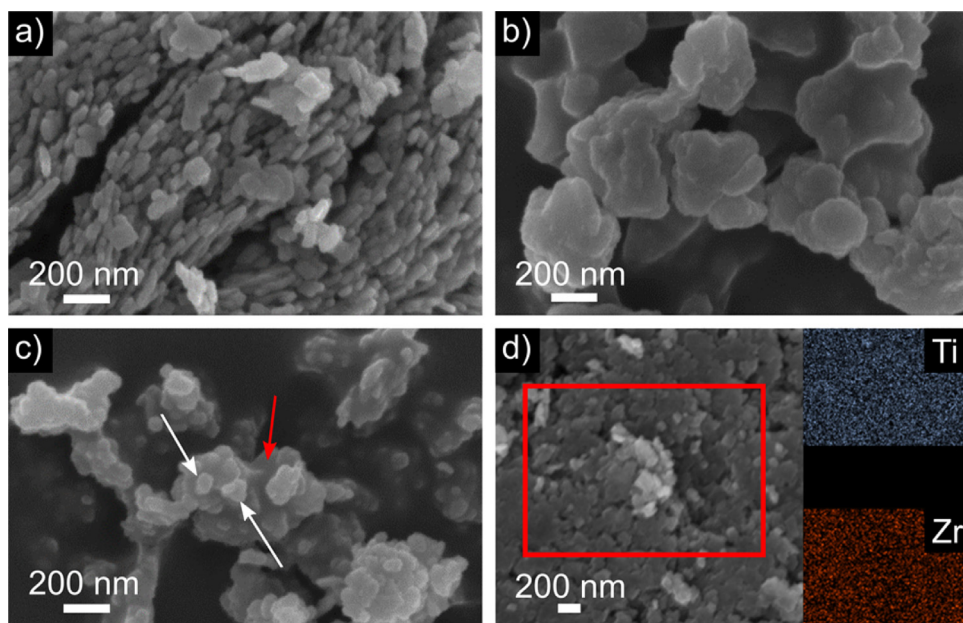


Fig. 4. SEM images of: (a) TiO_2 , (b) $\text{NH}_2\text{-UiO-66}$, (c) 2-TiMOF with TiO_2 particles (white arrows) and $\text{NH}_2\text{-UiO-66}$ particles (red arrow) indicated, and (d) EDX of 2-TiMOF with zirconium and titanium element mapping showing the homogenous nature of the composites. (For interpretation of the references to colour in this figure legend, the reader is referred to the web version of this article.)

and confirmed an interaction between the TiO_2 and $\text{NH}_2\text{-UiO-66}$ with a possible formation of an effective path for charge carrier migration. Based on the obtained Zr/Ti surface atomic ratio equal to 0.42 it can be concluded that although most of the TiO_2 NS is incorporated within the inner part of the MOF particles, part of the TiO_2 particles is also present at the surface of the composite. The C 1s, O 1s and N 1s peaks are shown in Fig. S4. In the C 1s spectra the component at ca. 288.5 eV, that is due to sp^2C atoms bonding to N or O=C=O [49,50], is enhanced in MOF and 2-TiMOF as compared to the pure TiO_2 . Similarly, the O 1s peak at 529.4 eV, attributed to the lattice oxygen ions of the TiO_2 network, is shifted by ca. 0.2 eV to higher BE in the nanocomposite

By visualizing the morphology of the composites, SEM brought further evidence of the formation of composites (Fig. 4). As seen in Fig. 4a, pure TiO_2 presented a nanoplate morphology with an average side length of ca. 105 nm and thickness of ca. 32 nm (size estimated from 50 particles). These were observed in the form of agglomerates formed through the stacking of TiO_2 NS. At this point, it is highlighted the deviation from the typical octahedral bipyramidal morphology observed for natural anatase [51]. This is attributed to the presence of F^- ions (HF used for TiO_2 synthesis) controlling the morphology and favoring the growth of [001] facets [12,14]. The pure $\text{NH}_2\text{-UiO-66}$ (Fig. 4b) exhibited very smooth and clean surfaces presenting an average particle size of ca. 400 nm, similar to those reported previously for that material. [26,52,53] The nanocomposites exhibited features intermediate between those of pure TiO_2 and $\text{NH}_2\text{-UiO-66}$ (Fig. 4c). The presence of TiO_2 during the MOF synthesis created a composite material with an uneven and rough surface. This might be due to the fact that the presence of the TiO_2 nanoparticles modified the formation process of the MOF particles. Small TiO_2 nanoparticles could be clearly observed on the composites as indicated by the white arrows in Fig. 4c. What is more important to notice is that there was a uniform distribution of TiO_2 NS within the MOF structure. This was further confirmed by EDX (Fig. 4d), which highlighted the even dispersion of Ti and Zr atoms throughout the composite structure. Of importance is to mention that compared with the pure TiO_2 , no agglomerates or isolated TiO_2 particles were detected in the nanocomposites, verifying the initial hypothesis of using large TiO_2 nanoparticles. Overall, the SEM data

confirmed the successful formation of heterostructures and suggested a tight interaction between the two parts with a possible formation of a heterojunction.

As explained above, one of the key aspects of the use of MOFs in building the composites was to create the porosity necessary to capture CO_2 and also to favor access of CO_2 molecules to the catalytic sites. Hence the porosity of the materials was evaluated using nitrogen sorption isotherms (Fig. S5). Table 1 summarizes the BET surface area, pore volume and CO_2 adsorption capacity (obtained at 1 bar, 25 °C). As expected, the surface area of TiO_2 was found to be very low when compared to $\text{NH}_2\text{-UiO-66}$ with values similar to those reported, exhibiting typical adsorption/desorption isotherm features of a mesoporous material [23,35]. The nanocomposites contained micropores owing to the presence of $\text{NH}_2\text{-UiO-66}$ and their surface increased linearly with increasing $\text{NH}_2\text{-UiO-66}$ content. Overall, surface area based on the total weight of the nanocomposite was significantly lower than that of the pure $\text{NH}_2\text{-UiO-66}$ ($871 \text{ m}^2 \text{ g}^{-1}$). This was expected taking into consideration the low content of the MOF in the final composites. In fact, the experimentally observed surface area values of the nanocomposites were similar to the theoretical values – calculated by linear combination of their constituents surface area values using the content extracted from TGA (Table S2). Of importance is to mention that the mesoporous volumes for all composites were higher than those of both TiO_2 and $\text{NH}_2\text{-UiO-66}$. This must originate from the incorporation of the TiO_2 nanoparticles within the MOF structure. Indeed, the composites were prepared in such a way that the MOF synthesis took place in the presence of TiO_2 nanoparticles. As a result, the MOF crystal growth might have been affected, especially at the interface between the TiO_2 particles and the MOF particles. This could lead to missing ligands in the MOF that in turn caused an increase in the mesopores volume. On the other hand, the microporosity was not significantly altered when normalized to the MOF content.

As the porosity of the composites was confirmed, the amount of CO_2 captured was then investigated (Fig. 5, Table 1). The nanocomposites presented moderate adsorption capacity (ranging from 0.32 to 0.56 mmol g^{-1}) when compared with the pure $\text{NH}_2\text{-UiO-66}$ (1.30 mmol g^{-1}). However, CO_2 uptake was significantly improved

Table 1

Textural parameters derived from N₂ sorption isotherms at –196 °C along with CO₂ adsorption capacities at 1 bar and 25 °C for TiO₂, NH₂-UiO-66 and TiO₂/NH₂-UiO-66 composites.

	BET (m ² g ⁻¹)	V _{Tot} ^a (cm ³ g ⁻¹)	V _{Meso} ^b (cm ³ g ⁻¹)	V _{Micro} ^c (cm ³ g ⁻¹)	CO ₂ ad ^d (mmol g ⁻¹)	X _{TiO2} (% mass)
TiO ₂	42	0.149	0.149	–	0.061	100.0
1-TiMOF	173	0.213	0.173	0.040	0.32	81.0
2-TiMOF	202	0.233	0.184	0.049	0.36	80.5
3-TiMOF	268	0.236	0.165	0.071	0.47	75.5
4-TiMOF	284	0.215	0.138	0.077	0.56	63.2
NH ₂ -UiO-66	871	0.410	0.135	0.275	1.30	0.0

^a Calculated from the volume adsorbed at P/P₀ = 0.97.

^b Calculated from V_{meso} = V_{total} – V_{micro}.

^c Calculated from the t-plot method.

^d CO₂ adsorption capacity measured at 25 °C and 1 bar.

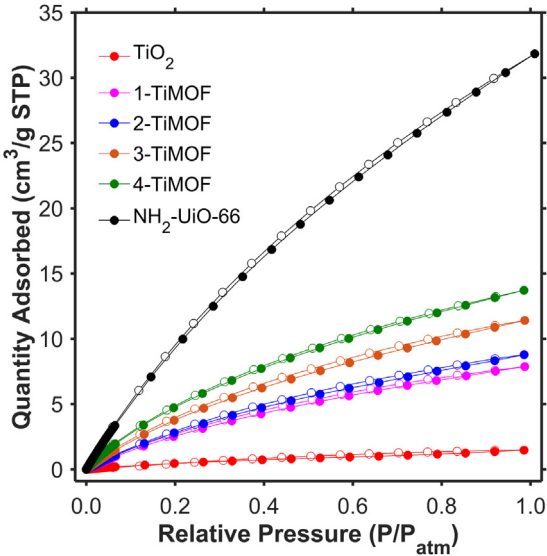


Fig. 5. CO₂ sorption isotherms measured at 25 °C for TiO₂, NH₂-UiO-66 and TiO₂/NH₂-UiO-66 composites (x-TiMOF).

when compared with the pure TiO₂ nanoparticles (0.061 mmol g⁻¹) and increased linearly with increasing MOF content. Hence, CO₂ adsorption on the nanocomposites was attributed to the presence of NH₂-UiO-66. This is also supported by the CO₂ adsorption capacity of the x-TiMOF materials normalized to the NH₂-UiO-66 content, which is approximately equal to that of NH₂-UiO-66. These results clearly indicate that the incorporation of TiO₂ into the structure did not inhibit CO₂ uptake by the MOF. The observed enhanced CO₂ adsorption by the nanocomposites compared with the pure TiO₂ may have an impact in photoactivity by increasing the CO₂ concentration on the photocatalyst surface [28].

3.2. Optical and photophysical properties of the materials and photocatalytic CO₂ reduction

As the materials were subsequently tested for the photocatalytic reduction of CO₂, their optical absorption properties were studied by DR-UV/Vis. The converted UV-vis absorption spectra are given Fig. S6a and the corresponding Tauc plots used to estimate the E_g values in Fig. S6b. TiO₂ was treated as indirect and NH₂-UiO-66 as direct semiconductor [51,54,55]. The absorption edge of the pure TiO₂ was around 380 nm while for the pure NH₂-UiO-66 the absorbance was extended up to 440 nm. These correspond to E_g values of 3.20 eV and 2.70 eV, respectively [27,51]. Regarding the nanocomposites, an obvious shift of the absorption band towards visible wavelengths was detected which can be exclusively attributed to the presence NH₂-UiO-66.

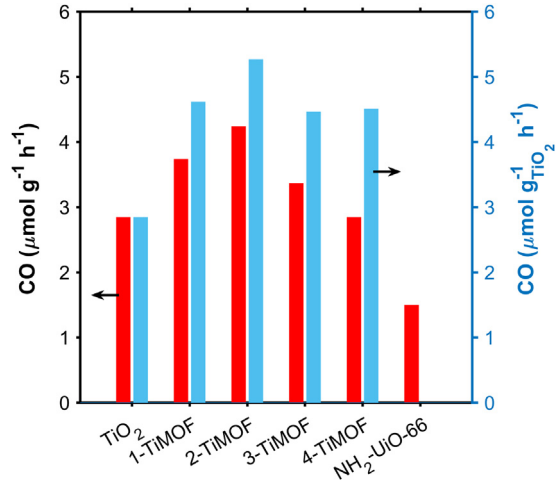


Fig. 6. Photocatalytic CO evolution from TiO₂, NH₂-UiO-66 and TiO₂/NH₂-UiO-66 composites (x-TiMOF).

The photocatalytic activity of the prepared materials was then evaluated against the gas phase photocatalytic reduction of CO₂ at ambient temperature using H₂ as a sacrificial agent. Under the conditions of the experiment, only CO was detected as a product in the gas phase. Fig. 6 presents the CO evolution at 6 h reaction time under UV-vis irradiation. The pure NH₂-UiO-66 presented the lowest activity. Recently, NH₂-UiO-66 [23] as well as other amino-functionalized [56] and Zr-cluster containing MOFs [57] have been proven active for CO₂ reductions but reactions have been carried out in the liquid phase using light irradiation of higher power. Here, a gas/solid phase set-up was selected to mimic the conditions needed for a combined CO₂ capture and CO₂ conversion process as a way towards carbon management. In the case of the TiO₂-based materials, all nanocomposites showed superior photoactivity compared with the pure TiO₂ indicating a synergistic effect between TiO₂ and NH₂-UiO-66 (red bars in Fig. 6). CO evolution first increased and then declined with increasing MOF content. The nanocomposite containing moderate amount of NH₂-UiO-66 (ca. 20 wt.%) presented the highest activity, i.e. 1.5 times more active than the pure TiO₂. This enhancement was all the more evidenced on the basis of TiO₂ total mass. Indeed, when photoactivity was normalized to the TiO₂ content determined by TGA (blue bars in Fig. 6), the optimum 2-TiMOF nanocomposite exhibited approximately 1.9 times increased CO evolution rate compared with the pure TiO₂. At this point of importance is to mention that no CO₂ reduction was observed over CdS/NH₂UiO-66 composites although CdS coupled with other MOF was proven active under the same conditions [24]. The difference in the findings of the present study and in ref [24] highlight the importance of the proper choice of the

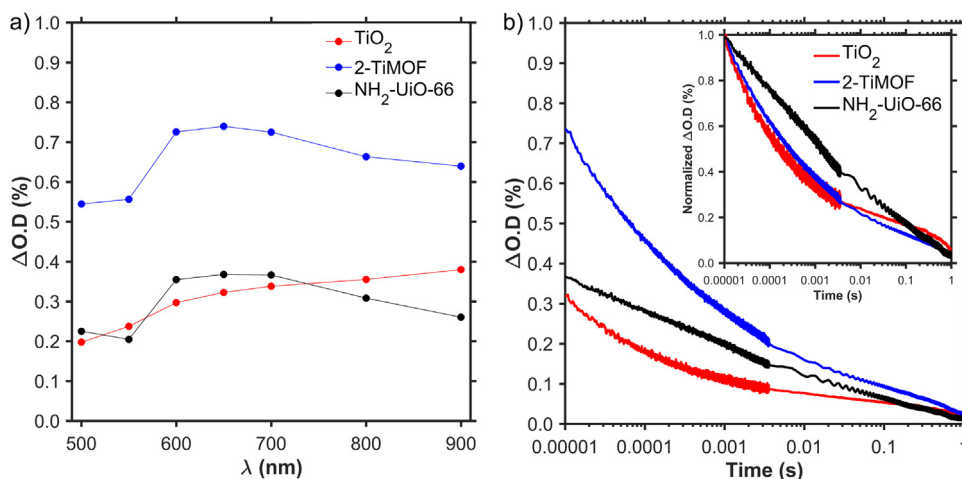


Fig. 7. Transient absorption spectroscopy study of TiO₂, NH₂-UiO-66 and TiO₂/NH₂-UiO-66 composite (2-TiMOF): (a) transient absorption spectrum 10 μ s after a laser pulse, and (b) kinetics of charge carrier recombination at 650 nm, with the normalized kinetics shown inset ($\lambda_{\text{exc}} = 355$ nm, ~ 2 mJ.cm $^{-2}$, 6 ns pulse width, $0.6 = 355$ nm, ~ 2 mJ.cm $^{-2}$, 6 ns pulse width, 0.6 Hz).

individual parts for the development of composites, i.e. allowing spontaneous electron transfer to the active phase.

In order to establish the contribution of a heterojunction formation in photoactivity, a physical mixture containing the same weight ratio of TiO₂ and NH₂-UiO-66 as that of the 2-TiMOF nanocomposite was prepared and tested. The activity of the mechanically mixed sample resembled that of TiO₂. This indicates that the *in-situ* process applied herein for the synthesis of the nanocomposites is prerequisite for the development of an interfacial interaction between the two components, which in turn has a crucial role in activity. It is highlighted that no CO was detected in all reference reactions carried out in the dark, the absence of catalyst or under N₂/H₂ atmosphere. These results clearly indicate that CO originated from the photocatalytic reduction of CO₂. In terms of catalyst stability, the CO evolution from 2-TiMOF was observed to proceed at a near constant rate over the 6 h testing period (Fig. S7). In addition, catalytic reactions were conducted to evaluate the stability of the prepared materials. No apparent decrease in CO evolution was detected when using the same catalyst for three consecutive times highlighting the stability of the prepared materials under the conditions used (Fig. S8). Stability was further verified by acquiring the XRD patterns of the used catalysts. The XRD patterns of the materials remained unaltered after the reaction, further verifying the robustness of the materials (Fig. S9).

There are different and non-exclusive factors that could account for the enhanced CO₂ reduction observed over the prepared nanocomposites. The MOF can act as an interface spacer preventing agglomeration of TiO₂ nanoparticles and providing additional exposed surface facilitating activity. This was evidenced by SEM in the prepared nanocomposites (Fig. 4). The observed superior CO₂ uptake of the nanocomposites vs. the pure TiO₂ could also improve photoactivity [28] via increasing the CO₂ levels close to the photoactive surfaces. Light absorption properties of the prepared nanocomposites were also improved. The absorption edge of the TiO₂/NH₂-UiO-66 nanocomposites was red-shifted by approximately 70 nm compared to the pure TiO₂ NS. However, light absorption and CO₂ adsorption alone cannot interpret the observed trend in the nanocomposite series since 4-TiMOF was less active than 2-TiMOF. Regarding the actual trend in CO evolution rate observed within the TiO₂/NH₂-UiO-66 samples, as TiO₂ was the most active phase of CO₂ photoreduction process (Fig. 6), the drop of photoactivity at high MOF loadings might be related to the decrease of the most photoactive phase, i.e. the TiO₂. Alternatively, considering that both phases (TiO₂ and MOF) are photoexcited

under the applied conditions, excess NH₂-UiO-66 may have also decreased the number of hetero-interfaces in the nanocomposites, which in turn disfavored charge transfer process in heterostructures [58].

It is well known that among the different factors determining photoactivity, both the ability to produce photogenerated charges but also their efficient separation are considered essential [59]. Herein, in an effort to determine the electronic properties related with activity, transient absorption spectra were recorded in order to evaluate charge transfer processes.

Transient absorption spectroscopy (TAS) is a form of laser flash spectroscopy that can monitor the generation, recombination, trapping and charge transfer events of photogenerated charges in semiconductors [60–62]. The dynamics specific to photogenerated electrons or holes can be studied by tracking transient changes in absorbance at particular wavelengths [63]. This technique has primarily been used to study charge transfer processes in solar cells [64,65] but has also been used to study charge transfers in composite photocatalysts [66] and also the kinetics of photocatalytic processes [39,67]. For this study, TAS measurements were focused on long lived charge carriers (micro- to millisecond), as it has been shown that these are the timescales most relevant to CO₂ reduction kinetics (typically several hundred microseconds) [17].

The transient change in absorption, 10 μ s after a laser pulse, is shown in Fig. 7a. TiO₂ sample displayed a rather broad spectrum that increased in absorption into the near-IR, while the pure NH₂-UiO-66 MOF showed a more structured spectrum, with a maximum absorption at ~ 650 nm. The composite, 2-TiMOF, exhibited a spectral signature almost identical to that of the pure MOF. Considering the composite was mostly composed of TiO₂ (approximately 80% TiO₂ and 20% NH₂-UiO-66 MOF), the laser excitation would mostly be absorbed by the TiO₂ component. Hence, the spectral signature of the composite pointed to a charge transfer from TiO₂ sites to the MOF. Previous TAS studies of TiO₂ have shown that transient absorption is dominated by the absorption of photogenerated holes in the visible region [39]. This means that the change in the spectral signature of the composite was likely due to the transfer of a photogenerated holes in TiO₂ to the MOF. Charge transfer was the observed increase in transient absorption in the composite, which approximately doubled in comparison to either of its pure counterparts (Fig. 7a). However, photo-generated charges in the composite did not recombine more slowly than in the pure MOF, and in fact, recombined at a similar rate to the pure TiO₂ sample (Fig. 7b). We therefore attribute the increase in the num-

ber of charge carriers present in the composite to an inhibition of early timescale recombination. This was most likely caused by an increase in charge carrier separation due to charge transfer from TiO_2 sites into the MOF. On the micro- to millisecond timescales, recombination was slightly faster in the composite compared to the pure MOF. However, the number of charge carriers that remained present on timescales relevant to CO_2 reduction was superior in the composite. This correlated with our photocatalytic studies, which showed that the composite, 2-TiMOF, was significantly more active than either of its counterparts. More detailed results of our transient absorption studies are provided in the Supporting Information (Fig. S10)

Compared with previous transient absorption studies of MOFs, $\text{NH}_2\text{-UiO-66}$ and its composites (*vide-infra*) show substantially longer electron-hole lifetimes [68–71]. Previous studies have shown that the half-time for recombination in MOF-5 (Zn_4O clusters linked orthogonally to terephthalate) was $\sim 50 \mu\text{s}$ [68,69]. Substantially lower half-times ($\sim 8 \mu\text{s}$) were observed by Garcia et al. in CAU-8 (AlO_6 octahedra connected by benzophenone dicarboxylate linkers) [70]. Epitaxial films of SURMOF 2 (Zn_4O clusters linked to porphyrin rings) showed similarly fast electron-hole recombination [71]. In this work, $\text{NH}_2\text{-UiO-66}$ showed recombination half-times in the region of $1500 \mu\text{s}$, which were substantially longer lived than the pure TiO_2 sample ($\sim 180 \mu\text{s}$). Of note, previous TAS studies have also focused on the ultra-fast charge-carrier dynamics (from the femto- to nanosecond timescale) of MOF systems capable of reducing CO_2 [22,27]. Li et al. found that photogenerated electrons transferred from anatase TiO_2 to HKUST-1 within several picoseconds [27]. Also, Zhang et al. found that MOF-525 (composed of Zr_6 clusters and porphyrin-based molecular units) can transfer charge onto impregnated Co centres within 10 ps [22]. Herein, although no direct charge transfer at short timescale was observed, we did not observe directly such mechanism at short timescale, the data acquired on longer timescales (micro- to millisecond) suggest transfer of short lived charges.

3.3. Proposed photocatalytic pathway

Given the analysis above, a plausible mechanism for enhanced photocatalytic CO_2 reduction over the as synthesis $\text{TiO}_2/\text{NH}_2\text{-UiO-66}$ nanocomposites could be proposed. The conduction band potential of $\text{NH}_2\text{-UiO-66}$ has been reported to be -0.6 eV [72]. This was significantly more negative than the conduction band level of anatase TiO_2 (-0.28 eV) [73]. This combined with the E_g values determined by DR/UV-vis and the chemical interaction suggested by XPS, confirmed formation of a Type II heterojunction and allowed the full band structure to be illustrated. A schematic diagram of the band energy levels together with the suggested charge transfer driven by the band energy difference is given in Fig. 8.

Close inspection of the catalytic results (Fig. 6) suggested that although the light absorption and CO_2 uptake properties may have impacted photoactivity, they are not the sole factors governing the photocatalytic efficiency. TiO_2 must have had a crucial role in the photoactivity. On the basis of these observations and the charge transfer mechanism presented in Fig. 8, it is suggested that CO_2 is photocatalytically reduced to CO by TiO_2 . CO_2 reduction may have also occurred on $\text{NH}_2\text{-UiO-66}$ but to a lesser extent, as observed experimentally. In the $\text{TiO}_2/\text{NH}_2\text{-UiO-66}$ nanocomposites photoactivity was mainly governed by two parameters: (a) the content of TiO_2 that controls the available sites for CO_2 reduction and (b) the presence of $\text{NH}_2\text{-UiO-66}$ as charge separator and CO_2 adsorbent. The actual content of the two parts would control activity. However, improved catalytic activity is mainly attributed to the enhanced abundance of photogenerated charges driven by the interfacial charge transfer.

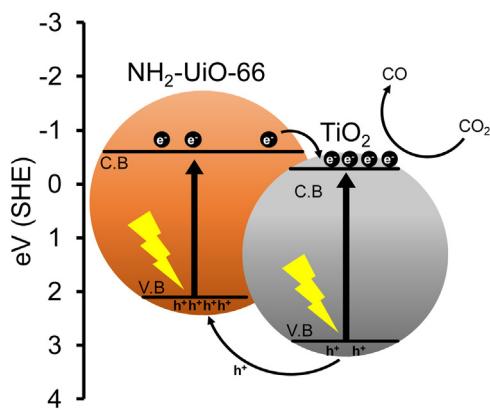


Fig. 8. Proposed photocatalytic CO_2 reduction pathway over $\text{TiO}_2/\text{NH}_2\text{-UiO-66}$. CO_2 is photocatalytically reduced to CO by TiO_2 , which is enhanced by interfacial charge transfer.

4. Conclusions

To conclude, $\text{TiO}_2/\text{NH}_2\text{-UiO-66}$ nanocomposites were synthesized for the first time via an *in-situ* process allowing intimate contact between the two components. As a result, the composites exhibited enhanced photocatalytic CO_2 reduction to CO in the presence of H_2 compared to the parent materials. $\text{TiO}_2/\text{NH}_2\text{-UiO-66}$ displayed several features that promoted catalytic activity. The composite heterostructures maintained a high surface area preventing TiO_2 aggregation and exposing more active sites. The large CO_2 adsorption capacity also increased the CO_2 level on the surface (owing to the presence of the MOF porosity), facilitating intimate contact of CO_2 with the photocatalytic sites. The optical properties of the composite were improved for the targeted reaction, with an absorption shift towards visible light compared to TiO_2 . Transient absorption spectroscopy revealed increased charge generation enabled by efficient charge transfer, resulting in additional photo-excited electrons. This study demonstrated photocatalytic CO_2 reduction over TiO_2 can be greatly improved with the use of $\text{NH}_2\text{-UiO-66}$ as CO_2 adsorbent and charge separator.

Acknowledgements

This work was supported by the Engineering and Physical Science Research Council through the First Grant scheme (EP/N024206/1) and via a Departmental Training Partnership grant.

Appendix A. Supplementary data

Supplementary data associated with this article can be found, in the online version, at <http://dx.doi.org/10.1016/j.apcatb.2017.03.039>.

References

- [1] R.K. Pachauri, L.A.e. Meyer, *Climate Change 2014: Synthesis Report. Contribution of Working Groups I, II and III to the Fifth Assessment Report of the Intergovernmental Panel on Climate Change* IPPC, IPCC, Geneva, Switzerland, 2014, 151 pp.
- [2] T. Kuramochi, A. Ramírez, W. Turkenburg, A. Faaij, Effect of CO_2 capture on the emissions of air pollutants from industrial processes, *Int. J. Greenh. Gas Control* 10 (2012) 310–328.
- [3] N. MacDowell, N. Florin, A. Buchard, J. Hallett, A. Galindo, G. Jackson, C.S. Adjiman, C.K. Williams, N. Shah, P. Fennell, An overview of CO_2 capture technologies, *Energy Environ. Sci.* 3 (2010) 1645–1669.
- [4] A. Samanta, A. Zhao, G.K.H. Shimizu, P. Sarkar, R. Gupta, Post-combustion CO_2 capture using solid sorbents: a review, *Ind. Eng. Chem. Res.* 51 (2012) 1438–1463.

- [5] K. Sumida, D.L. Rogow, J.A. Mason, T.M. McDonald, E.D. Bloch, Z.R. Herm, T.-H. Bae, J.R. Long, Carbon dioxide capture in metal–organic frameworks, *Chem. Rev.* 112 (2012) 724–781.
- [6] M. Mikkelsen, M. Jorgensen, F.C. Krebs, The teraton challenge. A review of fixation and transformation of carbon dioxide, *Energy Environ. Sci.* 3 (2010) 43–81.
- [7] A. Goeppert, M. Czaun, J.-P. Jones, G.K. Surya Prakash, G.A. Olah, Recycling of carbon dioxide to methanol and derived products – closing the loop, *Chem. Soc. Rev.* 43 (2014) 7995–8048.
- [8] T. Inoue, A. Fujishima, S. Konishi, K. Honda, Photoelectrocatalytic reduction of carbon dioxide in aqueous suspensions of semiconductor powders, *Nature* 277 (1979) 637–638.
- [9] Y. Izumi, Recent advances in the photocatalytic conversion of carbon dioxide to fuels with water and/or hydrogen using solar energy and beyond, *Coord. Chem. Rev.* 257 (2013) 171–186.
- [10] W. Fan, Q. Zhang, Y. Wang, Semiconductor-based nanocomposites for photocatalytic H₂ production and CO₂ conversion, *Phys. Chem. Chem. Phys.* 15 (2013) 2632–2649.
- [11] H. Xu, S. Ouyang, L. Liu, P. Reunchan, N. Umezawa, J. Ye, Recent advances in TiO₂-based photocatalysis, *J. Mater. Chem. A* 2 (2014) 12642–12661.
- [12] Y. Cao, Q. Li, C. Li, J. Li, J. Yang, Surface heterojunction between {001} and {101} facets of ultrafine anatase TiO₂ nanocrystals for highly efficient photoreduction CO₂ to CH₄, *Appl. Catal. B: Environ.* 198 (2016) 378–388.
- [13] X. Meng, S. Ouyang, T. Kako, P. Li, Q. Yu, T. Wang, J. Ye, Photocatalytic CO₂ conversion over alkali modified TiO₂ without loading noble metal cocatalyst, *Chem. Commun.* 50 (2014) 11517–11519.
- [14] J. Yu, J. Low, W. Xiao, P. Zhou, M. Jaroniec, Enhanced photocatalytic CO₂-reduction activity of anatase TiO₂ by coexposed {001} and {101} facets, *J. Am. Chem. Soc.* 136 (2014) 8839–8842.
- [15] K. Li, T. Peng, Z. Ying, S. Song, J. Zhang, Ag-loading on brookite TiO₂ quasi nanocubes with exposed {2 1 0} and {0 0 1} facets: activity and selectivity of CO₂ photoreduction to CO/CH₄, *Appl. Catal. B: Environ.* 180 (2016) 130–138.
- [16] S. Xie, Y. Wang, Q. Zhang, W. Deng, Y. Wang, MgO- and Pt-promoted TiO₂ as an efficient photocatalyst for the preferential reduction of carbon dioxide in the presence of water, *ACS Catal.* 4 (2014) 3644–3653.
- [17] C.D. Windle, E. Pastor, A. Reynal, A.C. Whitwood, Y. Vaynzof, J.R. Durrant, R.N. Perutz, E. Reisner, Improving the photocatalytic reduction of CO₂ to CO through immobilisation of a molecular Re catalyst on TiO₂, *Chem.—A Eur. J.* 21 (2015) 3746–3754.
- [18] Z. Xiong, Y. Luo, Y. Zhao, J. Zhang, C. Zheng, J.C.S. Wu, Synthesis, characterization and enhanced photocatalytic CO₂ reduction activity of graphene supported TiO₂ nanocrystals with coexposed {001} and {101} facets, *Phys. Chem. Chem. Phys.* 18 (2016) 13186–13195.
- [19] T. Zhang, W. Lin, Metal-organic frameworks for artificial photosynthesis and photocatalysis, *Chem. Soc. Rev.* 43 (2014) 5982–5993.
- [20] C.-C. Wang, Y.-Q. Zhang, J. Li, P. Wang, Photocatalytic CO₂ reduction in metal-organic frameworks: a mini review, *J. Mol. Struct.* 1083 (2015) 127–136.
- [21] Y. Lee, S.J. Kim, H. Fei, J.K. Kang, S.M. Cohen, Photocatalytic CO₂ reduction using visible light by metal-monocatecholate species in a metal-organic framework, *Chem. Commun.* (2015).
- [22] H. Zhang, J. Wei, J. Dong, G. Liu, L. Shi, P. An, G. Zhao, J. Kong, X. Wang, X. Meng, Efficient visible-xp-light-driven carbon dioxide reduction by a single-atom implanted metal–organic framework, *Angew. Chem.* (2016).
- [23] D. Sun, Y. Fu, W. Liu, L. Ye, D. Wang, L. Yang, X. Fu, Z. Li, Studies on photocatalytic CO₂ reduction over NH₂-UiO-66(Zr) and its derivatives: towards a better understanding of photocatalysis on metal–organic frameworks, *Chem.—A Eur. J.* 19 (2013) 14279–14285.
- [24] S. Wang, X. Wang, Photocatalytic CO₂ reduction by CdS promoted with a zeolitic imidazolate framework, *Appl. Catal. B: Environ.* 162 (2015) 494–500.
- [25] Y. Lee, S. Kim, J.K. Kang, S.M. Cohen, Photocatalytic CO₂ reduction by a mixed metal (Zr/Ti) mixed ligand metal-organic framework under visible light irradiation, *Chem. Commun.* (2015).
- [26] D. Sun, W. Liu, M. Qiu, Y. Zhang, Z. Li, Introduction of a mediator for enhancing photocatalytic performance via post-synthetic metal exchange in metal-organic frameworks (MOFs), *Chem. Commun.* 51 (2015) 2056–2059.
- [27] R. Li, J. Hu, M. Deng, H. Wang, X. Wang, Y. Hu, H.-L. Jiang, J. Jiang, Q. Zhang, Y. Xie, Y. Xiong, Integration of an inorganic semiconductor with a metal-organic framework: a platform for enhanced gaseous photocatalytic reactions, *Adv. Mater.* 26 (2014) 4783–4788.
- [28] M. Wang, D. Wang, Z. Li, Self-assembly of CPO-27-Mg/TiO₂ nanocomposite with enhanced performance for photocatalytic CO₂ reduction, *Appl. Catal. B: Environ.* 183 (2016) 47–52.
- [29] Q. Liu, Z.-X. Low, L. Li, A. Razmjou, K. Wang, J. Yao, H. Wang, ZIF-8/Zn₂GeO₄ nanorods with an enhanced CO₂ adsorption property in an aqueous medium for photocatalytic synthesis of liquid fuel, *J. Mater. Chem. A* 1 (2013) 11563–11569.
- [30] C. Wang, Z. Xie, K.E. deKrafft, W. Lin, Doping metal-organic frameworks for water oxidation, carbon dioxide reduction, and organic photocatalysis, *J. Am. Chem. Soc.* 133 (2011) 13445–13454.
- [31] D. Sun, Y. Gao, J. Fu, X. Zeng, Z. Chen, Z. Li, Construction of a supported Ru complex on bifunctional MOF-253 for photocatalytic CO₂ reduction under visible light, *Chem. Commun.* (2015).
- [32] S. Yan, S. Ouyang, H. Xu, M. Zhao, X. Zhang, J. Ye, Co-ZIF-9/TiO₂ nanostructure for superior CO₂ photoreduction activity, *J. Mater. Chem. A* (2016).
- [33] J. Hong, C. Chen, F.E. Bedoya, G.H. Kelsall, D. O'Hare, C. Petit, Carbon nitride nanosheet/metal-organic framework nanocomposites with synergistic photocatalytic activities, *Catal. Sci. Technol.* 6 (2016) 5042–5051.
- [34] X. Han, Q. Kuang, M. Jin, Z. Xie, L. Zheng, Synthesis of titania nanosheets with a high percentage of exposed {001} facets and related photocatalytic properties, *J. Am. Chem. Soc.* 131 (2009) 3152–3153.
- [35] M.J. Katz, Z.J. Brown, Y.J. Colon, P.W. Siu, K.A. Scheidt, R.Q. Snurr, J.T. Hupp, O.K. Farha, A facile synthesis of UiO-66, UiO-67 and their derivatives, *Chem. Commun.* 49 (2013) 9449–9451.
- [36] W. Luo, S. Zafeiratos, Tuning morphology and redox properties of cobalt particles supported on oxides by an in between graphene layer, *J. Phys. Chem. C* 120 (2016) 14130–14139.
- [37] S. Brunauer, P.H. Emmett, E. Teller, Adsorption of gases in multimolecular layers, *J. Am. Chem. Soc.* 60 (1938) 309–319.
- [38] P.C. Rao, A.K.S. Mandal, Synthesis, structure and band gap energy of a series of thermostable alkaline earth metal based metal-organic frameworks, *CrystEngComm* 16 (2014) 9320–9325.
- [39] X. Wang, A. Kafizas, X. Li, S.J. Moniz, P.J. Reardon, J. Tang, I.P. Parkin, J.R. Durrant, Transient absorption spectroscopy of anatase and rutile: the impact of morphology and phase on photocatalytic activity, *J. Phys. Chem. C* 119 (2015) 10439–10447.
- [40] E.H. Otal, M.L. Kim, M.E. Calvo, L. Karvonen, I.O. Fabregas, C.A. Sierra, J.P. Hinestrosa, A panchromatic modification of the light absorption spectra of metal-organic frameworks, *Chem. Commun.* 52 (2016) 6665–6668.
- [41] S. Yin, H. Yamaki, M. Komatsu, Q. Zhang, J. Wang, Q. Tang, F. Saito, T. Sato, Preparation of nitrogen-doped titania with high visible light induced photocatalytic activity by mechanochemical reaction of titania and hexamethylenetetramine, *J. Mater. Chem.* 13 (2003) 2996–3001.
- [42] X. Wang, L. Xie, K.-W. Huang, Z. Lai, A rationally designed amino-borane complex in a metal organic framework: a novel reusable hydrogen storage and size-selective reduction material, *Chem. Commun.* 51 (2015) 7610–7613.
- [43] M. Kandiah, S. Usseglio, S. Svelle, U. Olsbye, K.P. Lillerud, M. Tilset, Post-synthetic modification of the metal-organic framework compound UiO-66, *J. Mater. Chem.* 20 (2010) 9848–9851.
- [44] J.H. Cavka, S. Jakobsen, U. Olsbye, N. Guillou, C. Lamberti, S. Bordiga, K.P. Lillerud, A new zirconium inorganic building brick forming metal organic frameworks with exceptional stability, *J. Am. Chem. Soc.* 130 (2008) 13850–13851.
- [45] S. Chu, Y. Wang, Y. Guo, J. Feng, C. Wang, W. Luo, X. Fan, Z. Zou, Band structure engineering of carbon nitride: in search of a polymer photocatalyst with high photooxidation property, *ACS Catal.* 3 (2013) 912–919.
- [46] L. Schlur, S. Begin-Colin, P. Gilliot, M. Gallart, G. Carré, S. Zafeiratos, N. Keller, V. Keller, P. André, J.-M. Grenche, B. Hezard, M.-H. Desmonts, G. Pourroy, Effect of ball-milling and Fe-/Al-doping on the structural aspect and visible light photocatalytic activity of TiO₂ towards Escherichia coli bacteria abatement, *Mater. Sci. Eng.: C* 38 (2014) 11–19.
- [47] V. Papaefthimiou, T. Dintzer, M. Lebedeva, D. Teschner, M. Hävecker, A. Knop-Gericke, R. Schlögl, V. Pierron-Bohnes, E. Savinova, S. Zafeiratos, Probing metal–support interaction in reactive environments: an in situ study of Pt/Co bimetallic nanoparticles supported on TiO₂, *J. Phys. Chem. C* 116 (2012) 14342–14349.
- [48] S. Zafeiratos, S. Kennou, Gold/nickel ultrathin bimetallic overlayers on yttria-stabilized ZrO₂ (100), *J. Phys. Chem. B* 106 (2002) 41–48.
- [49] Y. Chen, B. Wang, S. Lin, Y. Zhang, X. Wang, Activation of n → π* transitions in two-dimensional conjugated polymers for visible light photocatalysis, *J. Phys. Chem. C* 118 (2014) 29981–29989.
- [50] G. Beamson, D. Briggs, High Resolution XPS of Organic Polymers, Wiley, 1992.
- [51] K.C. Christoforidis, A. Iglesias-Juez, S.J.A. Figueroa, M. Di Michiel, M.A. Newton, M. Fernandez-Garcia, Structure and activity of iron-doped TiO₂-anatase nanomaterials for gas-phase toluene photo-oxidation, *Catal. Sci. Technol.* 3 (2013) 626–634.
- [52] L.-L. Tan, H. Li, Y. Zhou, Y. Zhang, X. Feng, B. Wang, Y.-W. Yang, Zn²⁺-triggered drug release from biocompatible zirconium MOFs equipped with supramolecular gates, *Small* 11 (2015) 3807–3813.
- [53] M.W. Anjum, F. Verwoortele, A.L. Khan, B. Bueken, D.E. De Vos, I.F.J. Vankelecom, Modulated uiO-66-based mixed-matrix membranes for CO₂ separation, *ACS Appl. Mater. Interfaces* 7 (2015) 25193–25201.
- [54] L. Valenzano, B. Civalleri, S. Chavan, S. Bordiga, M.H. Nilsen, S. Jakobsen, K.P. Lillerud, C. Lamberti, Disclosing the complex structure of UiO-66 metal organic framework: a synergic combination of experiment and theory, *Chem. Mater.* 23 (2011) 1700–1718.
- [55] Y. Su, Z. Zhang, H. Liu, Y. Wang, Cd_{0.2}Zn_{0.85}@UiO-66-NH₂ nanocomposites as efficient and stable visible-light-driven photocatalyst for H₂ evolution and CO₂ reduction, *Appl. Catal. B: Environ.* 200 (2017) 448–457.
- [56] D. Wang, R. Huang, W. Liu, D. Sun, Z. Li, Fe-based MOFs for photocatalytic CO₂ reduction: role of coordination unsaturated sites and dual excitation pathways, *ACS Catal.* (2014) 4254–4260.
- [57] H.-Q. Xu, J. Hu, D. Wang, Z. Li, Q. Zhang, Y. Luo, S.-H. Yu, H.-L. Jiang, Visible-light photoreduction of C in a metal–organic framework: boosting electron–hole separation via electron trap states, *J. Am. Chem. Soc.* (2015) O2.
- [58] L. Sun, Y. Qi, C.-J. Jia, Z. Jin, W. Fan, Enhanced visible-light photocatalytic activity of g-C₃N₄/Zn₂GeO₄ heterojunctions with effective interfaces based on band match, *Nanoscale* 6 (2014) 2649–2659.
- [59] K.C. Christoforidis, M. Melchionna, T. Montini, D. Papoulis, E. Stathatos, S. Zafeiratos, E. Kordouli, P. Fornasiero, Solar and visible light photocatalytic

- enhancement of halloysite nanotubes/g-C₃N₄ heteroarchitectures, RSC Adv. 6 (2016) 86617–86626.
- [60] S.R. Pendlebury, X. Wang, F. Le Formal, M. Cornuz, A. Kafizas, S.D. Tilley, M. Grätzel, J.R. Durrant, Ultrafast charge carrier recombination and trapping in hematite photoanodes under applied bias, J. Am. Chem. Soc. 136 (2014) 9854–9857.
- [61] F.M. Pesci, A.J. Cowan, B.D. Alexander, J.R. Durrant, D.R. Klug, Charge carrier dynamics on mesoporous WO₃ during water splitting, J. Phys. Chem. Lett. 2 (2011) 1900–1903.
- [62] Y. Ma, S.R. Pendlebury, A. Reynal, F. Le Formal, J.R. Durrant, Dynamics of photogenerated holes in undoped BiVO₄ photoanodes for solar water oxidation, Chem. Sci. 5 (2014) 2964–2973.
- [63] A. Fujishima, X. Zhang, D.A. Tryk, TiO₂ photocatalysis and related surface phenomena, Surf. Sci. Rep. 63 (2008) 515–582.
- [64] L. Wang, C. McCleese, A. Kovalsky, Y. Zhao, C. Burda, Femtosecond time-resolved transient absorption spectroscopy of CH₃NH₃PbI₃ perovskite films: evidence for passivation effect of PbI₂, J. Am. Chem. Soc. 136 (2014) 12205–12208.
- [65] T.M. Clarke, F.C. Jamieson, J.R. Durrant, Transient absorption studies of bimolecular recombination dynamics in polythiophene/fullerene blend films, J. Phys. Chem. C 113 (2009) 20934–20941.
- [66] L. Wang, H.-Y. Wang, B.-R. Gao, L.-Y. Pan, Y. Jiang, Q.-D. Chen, W. Han, H.-B. Sun, Transient absorption spectroscopic study on band-structure-type change in CdTe/CdS core-shell quantum dots, IEEE J. Quantum Electron. 47 (2011) 1177–1184.
- [67] S. Devahasdin, C. Fan, K. Li, D.H. Chen, TiO₂ photocatalytic oxidation of nitric oxide: transient behavior and reaction kinetics, J. Photochem. Photobiol. A: Chem. 156 (2003) 161–170.
- [68] M. Alvaro, E. Carbonell, B. Ferrer, F.X. Llabrés i Xamena, H. Garcia, Semiconductor behavior of a metal-organic framework (MOF), Chem.—A Eur. J. 13 (2007) 5106–5112.
- [69] T. Tachikawa, J.R. Choi, M. Fujitsuka, T. Majima, Photoinduced charge-transfer processes on MOF-5 nanoparticles: elucidating differences between metal-organic frameworks and semiconductor metal oxides, J. Phys. Chem. C 112 (2008) 14090–14101.
- [70] H.G. Baldovi, M. Krüger, H. Reinsch, M. Alvaro, N. Stock, H. Garcia, Transient absorption spectroscopy and photochemical reactivity of CAU-8, J. Mater. Chem. C 3 (2015) 3607–3613.
- [71] J. Liu, W. Zhou, J. Liu, I. Howard, G. Kilibarda, S. Schlabach, D. Coupry, M. Addicoat, S. Yoneda, Y. Tsutsui, Photoinduced charge-carrier generation in epitaxial MOF thin films: high efficiency as a result of an indirect electronic band gap? Angew. Chem. Int. Ed. 54 (2015) 7441–7445.
- [72] L. Shen, S. Liang, W. Wu, R. Liang, L. Wu, CdS-decorated UiO-66(NH₂) nanocomposites fabricated by a facile photodeposition process: an efficient and stable visible-light-driven photocatalyst for selective oxidation of alcohols, J. Mater. Chem. A 1 (2013) 11473–11482.
- [73] D.O. Scanlon, C.W. Dunnill, J. Buckridge, S.A. Shevlin, A.J. Logsdail, S.M. Woodley, C.R.A. Catlow, M.J. Powell, R.G. Palgrave, I.P. Parkin, G.W. Watson, T.W. Keal, P. Sherwood, A. Walsh, A.A. Sokol, Band alignment of rutile and anatase TiO₂, Nat. Mater. 12 (2013) 798–801.